

## S1. DERIVATION OF DCI'S IMPEDANCE MODELING

$$\begin{aligned}
c_a[\pm f_p] = & (\mathbf{C}_{dq} - \omega_1 L_f \mathbf{I}_L) K(s_1) P_1(s_1) \\
& + 0.5(C_1(s_1) - A_1(s_1)) G_i(s_1) \\
& \pm 0.5j(D_1(s_1) - B_1(s_1)) G_i(s_1) \\
& - 0.5\omega_1 L_f B_1(s_1) \pm 0.5j\omega_1 L_f A_1(s_1) \\
& \mp 0.5j(C_1(s_1) - A_1(s_1)) G_i(s_1) K(s_3) P_2(s_3) \\
& \pm 0.5j\omega_1 L_f B_1(s_1) K(s_3) P_2(s_3) \\
& - 0.5(D_1(s_1) - B_1(s_1)) G_i(s_1) K(s_3) P_2(s_3) \\
& - 0.5\omega_1 L_f A_1(s_1) K(s_3) P_2(s_3) \\
& \mp 0.5j(C_2(s_3) - A_2(s_3)) G_i(s_3) K(s_1) P_1(s_1) \\
& \pm 0.5j\omega_1 L_f B_2(s_3) K(s_1) P_1(s_1) \\
& - 0.5(D_2(s_3) - B_2(s_3)) G_i(s_3) K(s_1) P_1(s_1) \\
& - 0.5\omega_1 L_f A_2(s_3) K(s_1) P_1(s_1)
\end{aligned} \tag{A1}$$

$$\begin{aligned}
c_a[\pm f_{p1}] = & (\mathbf{C}_{dq}^* - \omega_1 L_f \mathbf{I}_L^*) K(s_2) P_1(s_2) \\
& + 0.5(C_1(s_2) - A_1(s_2)) G_i(s_2) \\
& \mp 0.5j(D_1(s_2) - B_1(s_2)) G_i(s_2) \\
& - 0.5\omega_1 L_f B_1(s_2) \mp 0.5j\omega_1 L_f A_1(s_2) \\
& \pm 0.5j(C_1(s_2) - A_1(s_2)) G_i(s_2) K(s_4) P_2(s_4) \\
& \mp 0.5j\omega_1 L_f B_1(s_2) K(s_4) P_2(s_4) \\
& - 0.5(D_1(s_2) - B_1(s_2)) G_i(s_2) K(s_4) P_2(s_4) \\
& - 0.5\omega_1 L_f A_1(s_2) K(s_4) P_2(s_4) \\
& \pm 0.5j(C_2(s_4) - A_2(s_4)) G_i(s_4) K(s_2) P_1(s_2) \\
& \mp 0.5j\omega_1 L_f B_2(s_4) K(s_2) P_1(s_2) \\
& - 0.5(D_2(s_4) - B_2(s_4)) G_i(s_4) K(s_2) P_1(s_2) \\
& - 0.5\omega_1 L_f A_2(s_4) K(s_2) P_1(s_2)
\end{aligned} \tag{A2}$$

where  $\mathbf{C}_{dq} = \pm 0.5j(c_{d0} \pm j c_{q0})$ ;  $\mathbf{I}_L = 0.5I_L(\cos\varphi_{il} \pm j \sin\varphi_{il})$ ;  $s_1 = s \mp j2\pi f_1$ ;  $s_2 = s \pm j2\pi f_1$ ;  $s_3 = \pm j4\pi f_1$ ;  $s_4 = \mp j4\pi f_1$ .

From the derivation process, it can be observed that both  $c_a[\pm f_p]$  and  $c_{al}[\pm f_{p1}]$  are polynomials with respect to  $\mathbf{V}_p$ ,  $\mathbf{V}_{p1}$ ,  $\mathbf{I}_p$ ,  $\mathbf{I}_{p1}$ . By rearranging equations (A1) and (A2), the following expressions are obtained:

$$c_a[\pm f_p] = E_1 \mathbf{V}_p + E_2 \mathbf{V}_{p1} + E_3 \mathbf{I}_p + E_4 \mathbf{I}_{p1} \tag{A3}$$

$$c_{al}[\pm f_{p1}] = F_1 \mathbf{V}_p + F_2 \mathbf{V}_{p1} + F_3 \mathbf{I}_p + F_4 \mathbf{I}_{p1} \tag{A4}$$

where  $E_1$ ,  $E_2$ ,  $E_3$ ,  $E_4$ ,  $F_1$ ,  $F_2$ ,  $F_3$ ,  $F_4$  are defined as the polynomial coefficients of the corresponding terms.

Substituting equations (A3) and (A4) into equation (27), the final expression of the DCI's impedance can be derived as shown in equation (A5).

## S2. THEORETICAL BACKGROUND

To derive the impedance of a grid-connected converter using the harmonic linearization method, the time-domain variables must be transformed into their frequency-domain representations. The theoretical foundation of this process lies in the Fourier series expansion and the convolution theorem. Assume that the time-domain expression of a function  $x(t)$  is given by:

$$x(t) = x_1 \cos(2\pi f_1 t) + x_k \cos(2\pi f_k t + \phi_k) \tag{A6}$$

where  $x_1$  denotes the amplitude of the component at frequency  $f_1$ ,  $f_1$  is the fundamental frequency;  $x_k$  denotes the amplitude of the component at frequency  $f_k$ , and  $\phi_k$  is the initial phase angle.

The Fourier series expansion of  $x(t)$  is given by:

$$x(t) = \sum_{i=-\infty}^{\infty} \mathbf{X}[i] e^{j2\pi i t} \tag{A7}$$

where  $\mathbf{X}[i]$  is the Fourier coefficient of  $x(t)$ , which can be expressed as:

$$\mathbf{X}[i] = \begin{cases} \frac{x_1}{2}, & i = \pm f_1 \\ \frac{x_k}{2} e^{\pm \phi_k}, & i = \pm f_k \end{cases} \tag{A8}$$

As shown in Equation (A8), the time-domain expression  $x(t)$  is transformed into its frequency-domain representation  $\mathbf{X}[i]$  through the Fourier series expansion. Consequently, the complex mixture of frequency components in the time domain is converted into distinct and independent frequency components in the frequency domain, which facilitates the analysis and calculation of coupling and interactions among different frequencies.

The application of the convolution theorem in this paper is introduced as follows. Consider a time-domain function defined as the product of two functions, i.e.,

$$x(t) = x_1(t) \cdot x_2(t) \tag{A9}$$

Their respective Fourier coefficients satisfy the following convolution relationship:

$$x[i] = \sum_{k=-\infty}^{\infty} x_1[k] \cdot x_2[i-k] \tag{A10}$$

---


$$\begin{bmatrix} Z_{inv}^{pp} & Z_{inv}^{pn} \\ Z_{inv}^{np} & Z_{inv}^{nn} \end{bmatrix} = - \begin{bmatrix} K_m V_{dc} G_{del}(s) E_1 - Y_{con}(s) & K_m V_{dc} G_{del}(s) E_2 \\ K_m V_{dc} G_{del}(s - 2j\omega_1) F_1 & K_m V_{dc} G_{del}(s - 2j\omega_1) F_2 - Y_{con}(s - 2j\omega_1) \end{bmatrix}^{-1} \cdot \begin{bmatrix} sL_f - K_m V_{dc} G_{del}(s) E_3 & -K_m V_{dc} G_{del}(s) E_4 \\ -K_m V_{dc} G_{del}(s - 2j\omega_1) F_3 & (s - 2j\omega_1)L_f - K_m V_{dc} G_{del}(s - 2j\omega_1) F_4 \end{bmatrix} \tag{A5}$$

### 3. EXTENDED SYSTEM STABILITY ANALYSIS

#### A. The Operating Condition of Unbalanced Loads

This paper takes the case of  $S_{La} = S_{Lb} \neq S_{Lc}$  as an example to investigate the effects of variations in  $k_{pi}$ ,  $k_{pv}$ ,  $L_f$ , and  $L_g$  on the PMp under various degrees of load unbalance.  $S_{La}$ ,  $S_{Lb}$ , and  $S_{Lc}$  denote the apparent powers of phases A, B, and C, respectively. The coefficient  $k_L$  is defined as the ratio of the apparent power of the C-phase load relative to the A-phase load, as shown in (A11). A larger  $k_L$  means a higher level of load unbalance.

$$k_L = \frac{S_{Lc}}{S_{La}} \quad (\text{A11})$$

Fig. A1 demonstrates the impact of variations in  $k_{pi}$ ,  $k_{pv}$ ,  $L_f$ , and  $L_g$  on the PMp under different levels of load unbalance. The values of PMp are obtained from Equation (42),  $k_{pi}$  ranges from 0.6 to 6.0 with an interval of 0.2,  $k_{pv}$  ranges from 0.6 to 4.0 with an interval of 0.2,  $L_f$  ranges from 1 mH to 5 mH with an interval of 0.25 mH,  $L_g$  ranges from 1 mH to 10 mH with an interval of 0.5 mH, and  $k_L$  ranges from 1 to 6 with an interval of 1. The results presented in Fig. A1 are obtained under the parameter settings of  $S_{La} = S_{Lb} = (2000 + 500j)$  VA, and  $S_{Lc} = k_L S_{La}$ ; the other parameters are the same as those listed in Table 1.

Figs. A1(a) and A1(b) indicate that when  $k_L$  remains constant, increasing either  $k_{pi}$  or  $k_{pv}$  will enhance the stability margin of the grid-connected system. In contrast, when  $k_{pi}$  or  $k_{pv}$  is fixed, variations in  $k_L$  exert only a slight influence on the system stability margin; moreover, Figs. A1(c) and A1(d) indicate that when  $k_L$  remains constant, increasing  $L_g$  or decreasing  $L_f$  contributes to increasing the system stability margin. Similarly, when either  $L_f$  or  $L_g$  is fixed, changing  $k_L$  has only a negligible impact on system stability margin.

In general, the influence of  $k_L$  on the stability of grid-connected systems is relatively limited. This is primarily attributed to the fact that the impedance of the load is usually much greater than the grid impedance. Owing to the parallel configuration of the grid impedance and the load, the impedance characteristics on the grid side are mainly determined by the grid impedance. Therefore, variations in single-phase loads exert only a marginal effect on the grid-side impedance characteristics, resulting in a negligible impact on the PMp. To visually demonstrate the relationship between  $k_L$  and the stability margin of the droop-controlled grid-connected system, the stability regions for different values of  $k_{pi}$ ,  $k_{pv}$ ,  $L_f$ , and  $L_g$  are illustrated in Fig. A2. To maintain an adequate stability phase margin, the proportional gains of the current loop and voltage loop are chosen to satisfy  $k_{pi} \geq 1$  and  $k_{pv} \geq 1$ . In addition, the filter inductance is designed to satisfy  $1 \leq L_f \leq 3$  mH, while the grid inductance is required to meet  $L_g \geq 3$  mH. This corresponds to an SCR of 2.5, indicating a weak grid condition.

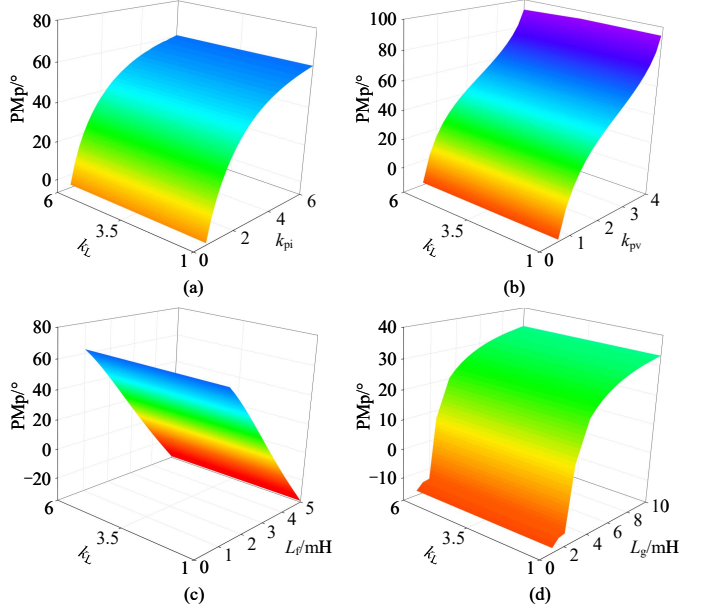


Fig. A1. Effect of  $k_{pi}$ ,  $k_{pv}$ ,  $L_f$  and  $L_g$  on the phase margin of the positive-sequence system under varying load unbalance degrees.

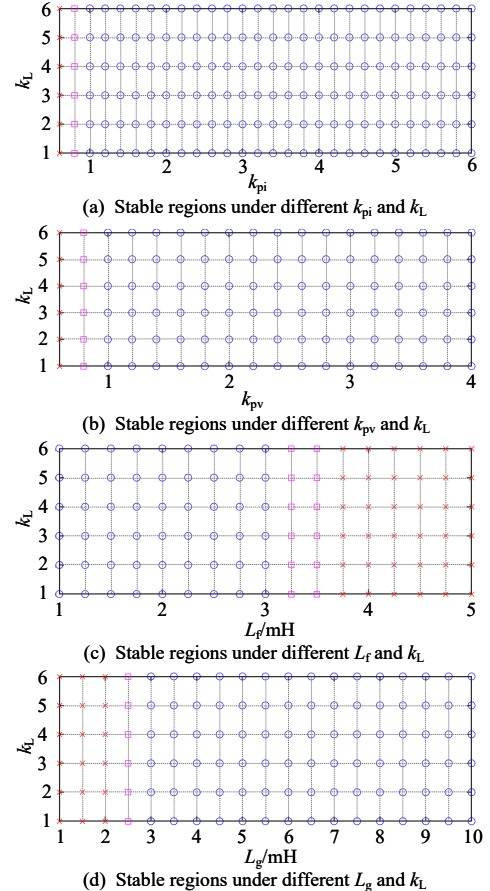


Fig. A2. Stable regions under different parameters and  $k_L$ .

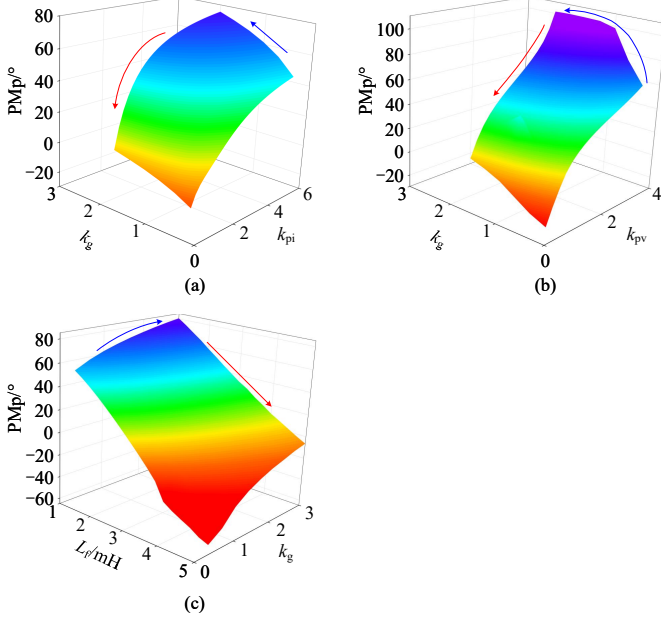


Fig. A3. Effect of  $k_{pi}$ ,  $k_{pv}$ , and  $L_f$  on the phase margin of the positive-sequence system under varying grid impedance unbalance degrees.

#### B. The Operating Condition of Unbalanced grid impedance

In this paper, the case of  $Z_{ga} = Z_{gb} \neq Z_{gc}$  is considered to analyze the impact of variations in  $k_{pi}$ ,  $k_{pv}$ , and  $L_f$  on the PMp under different levels of grid impedance unbalance,  $Z_{ga}$ ,  $Z_{gb}$ , and  $Z_{gc}$  represent the grid impedance of phases A, B, and C, respectively. The coefficient  $k_g$  is defined as the ratio of the C-phase grid impedance to the A-phase grid impedance, as shown in (A12).

$$k_g = \frac{Z_{gc}}{Z_{ga}} \quad (\text{A12})$$

Fig. A3 illustrates the influence of variations in  $k_{pi}$ ,  $k_{pv}$ , and  $L_f$  on the PMp under different levels of grid impedance unbalance. The values of PMp are obtained from Equation (42),  $k_{pi}$  ranges from 0.6 to 6.0 with an interval of 0.2,  $k_{pv}$  ranges from 0.6 to 4.0 with an interval of 0.2,  $L_f$  ranges from 1mH to 5mH with an interval of 0.25 mH, and  $k_g$  ranges from 1/3 to 3 with an interval of 1/3. The results presented in Fig. A3 are obtained under the parameter setting  $Z_{ga} = Z_{gb} = R_{ga} + j\omega_1 L_{ga}$ ,  $Z_{gc} = k_g Z_{ga}$ ,  $R_{ga} = 0.2 \Omega$ ,  $L_{ga} = 3 \text{ mH}$ , the other parameters are the same as those listed in Table 1.

As shown in Figs. A3(a) and A3(b), an increase in either  $k_{pi}$  or  $k_{pv}$  will enhance the stability margin of the grid-connected system when  $k_g$  is kept constant. When  $k_{pi}$  or  $k_{pv}$  is kept constant, the system's stability margin increases as  $k_g$  increases. A higher  $k_g$  value corresponds to a lower SCR for the C-phase, indicating a weaker grid condition for that phase. Furthermore, as illustrated in Fig. A3(c), when  $k_g$  is kept constant, the stability margin of the grid-connected system decreases as  $L_f$  increases. Conversely, when  $L_f$  is fixed, the stability margin increases as  $k_g$  becomes larger. In conclusion, under unbalanced grid impedance conditions, decreasing the

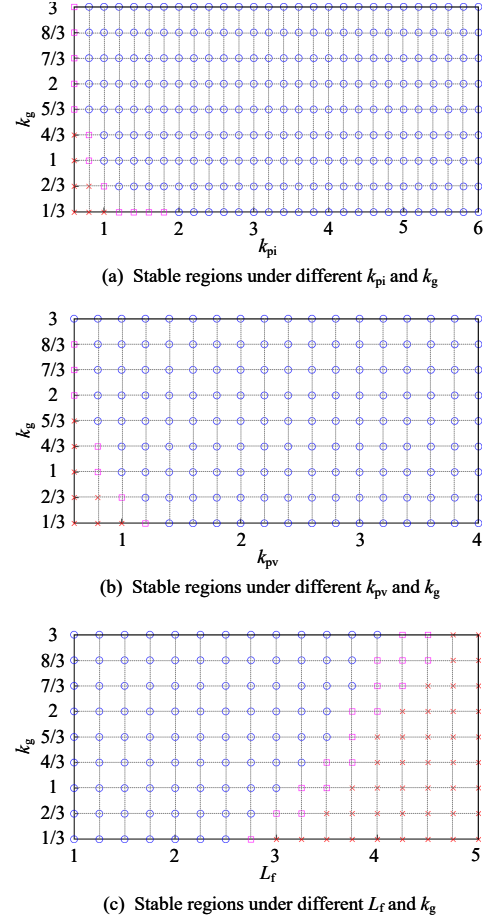


Fig. A4. Stable regions under different parameters and  $k_g$ .

SCR of one phase can enhance the overall stability margin. To visually demonstrate the relationship between  $k_g$  and the stability margin of the droop-controlled grid-connected system, the stability regions corresponding to different values of  $k_{pi}$ ,  $k_{pv}$ , and  $L_f$  are illustrated in Fig. A4. As shown in Fig. A4, the regions corresponding to critically stable and unstable parameter combinations gradually shrink with the increase of  $k_g$ , while the stable regions expand accordingly. This implies that the system's stability margin is improved even when one phase operates under weak-grid conditions.

#### C. Experimental Verification

Fig. A5 illustrates the experimental and theoretical analysis results of the effect of  $k_L$  variations on system stability. In Fig. A5(a)–(d), the three subplots from left to right represent the experimental waveform of PCC's voltages, the FFT result of the captured waveform, and the theoretical analysis of the oscillation frequency, respectively. As illustrated in Figs. A5(a)–(d), the system becomes unstable under the corresponding parameter settings, which is consistent with the analysis results presented in Fig. A2. In Fig. A5(a)–(d), the FFT analysis of the captured experimental waveform reveals the presence of both the oscillation frequencies and the corresponding coupling frequencies, which are in good agreement with the theoretical prediction. This indicates that the developed model can accurately capture the MFCE present during small-signal

TABLE A1  
THE PERFORMANCE OF THE FOUR MODELS IN CAPTURING THE MFCE (UNBALANCED GRID IMPEDANCE CONDITION)

(a)  $k_g = 1/3$ ,  $k_{pi} = 0.6$

Model	Theoretical oscillation frequency (deviation)	Theoretical mirror coupling frequency (deviation)
Model 1 [17]–[19]	26.4 Hz (−1.6 Hz)	73.6 Hz (+1.6 Hz)
Model 2 [20]–[22]	30.47 Hz (+2.47 Hz)	69.53 Hz (−2.47 Hz)
Model 3 [23]	28.02 Hz (+0.02 Hz)	71.98 Hz (−0.02 Hz)
Proposed model	27.99 Hz (−0.01 Hz)	72.01 Hz (+0.01 Hz)

*Note 1:* The actual oscillation frequency is 28 Hz, and the actual mirror coupling frequency is 72 Hz.

$k_g = 1/3$ ,  $k_{pv} = 0.8$

Model	Theoretical oscillation frequency (deviation)	Theoretical mirror coupling frequency (deviation)
Model 1 [17]–[19]	33.5 Hz (−2.5 Hz)	66.5 Hz (+2.5 Hz)
Model 2 [20]–[22]	35.09 Hz (−0.91 Hz)	64.91 Hz (+0.91 Hz)
Model 3 [23]	36 Hz (0 Hz)	64 Hz (0 Hz)
Proposed model	36.03 Hz (+0.03 Hz)	63.97 Hz (−0.03 Hz)

*Note 2:* The actual oscillation frequency is 36 Hz, and the actual mirror coupling frequency is 64 Hz.

(c)  $k_g = 1/3$ ,  $L_f = 3.5$  mH

Model	Theoretical oscillation frequency (deviation)	Theoretical mirror coupling frequency (deviation)
Model 1 [17]–[19]	32.62 Hz (−1.88 Hz)	67.38 Hz (+1.88 Hz)
Model 2 [20]–[22]	33.24 Hz (−1.26 Hz)	66.76 Hz (+1.26 Hz)
Model 3 [23]	34.45 Hz (−0.05 Hz)	65.55 Hz (+0.05 Hz)
Proposed model	34.53 Hz (+0.03 Hz)	65.47 Hz (−0.03 Hz)

*Note 3:* The actual oscillation frequency is 34.5 Hz, and the actual mirror coupling frequency is 65.5 Hz.

oscillations under unbalanced load conditions.

Similarly, Fig. A6 presents the experimental and theoretical analysis results of the effect of  $k_g$  variations on the system stability. In Fig. A6(a)–(c), the three subplots from left to right represent the FFT result of the captured waveform, the experimental waveform of PCC's voltages, and the theoretical analysis of the oscillation frequency, respectively. As illustrated in Fig. A6, the grid-connected system becomes unstable and exhibits oscillatory behavior when  $k_g = 1/3$  is combined with  $k_{pi} = 0.6$ ,  $k_{pv} = 0.6$ , or  $L_f = 3$  mH. The actual oscillation frequencies and the corresponding coupling frequencies are identified, as shown in the first sub-figure of Fig. A6(a)–(c), respectively, which agree well with the theoretical analysis results. When  $k_g$  increases to 3, the grid-connected system becomes stable in all three cases. This experimental observation agrees well with the theoretical analysis results shown in Fig. A4, confirming that a larger  $k_g$  improves the stability margin of the grid-connected system. In addition, the amplitudes of the fundamental positive-, negative-, and zero-sequence voltage components for  $k_g = 3$  are provided below Figs. A6(a)–(c).

#### S4. THE PERFORMANCE OF DIFFERENT MODELS IN CAPTURING MFCE

In this section, the unbalanced grid impedance condition is used as an illustrative example. The models derived from [17]–[19] (denoted as Model 1), [20]–[22] (denoted as Model 2), and [23] (denoted as Model 3) are compared with the proposed model in terms of their ability to capture the MFCE.

Table A1 summarizes the results shown in Figs. A6(a)–(c) of the proposed method and includes additional existing methods

for comparison, demonstrating their relative performance in capturing the MFCE under unbalanced grid impedance conditions. The actual oscillation frequencies and mirror coupling frequencies in Table A1 (a)–(c) are obtained from Fig. A6. As shown in Table A1, the proposed model is competitive with the model reported in [23], exhibiting a comparable level of frequency prediction precision in capturing the MFCE. Specifically, the deviations of the proposed model are limited to 0.01–0.03 Hz, indicating its high precision in MFCE prediction under unstable operating conditions. In contrast, Models 1 and 2 exhibit relatively larger errors in predicting the theoretical oscillation and mirror coupling frequencies.

Overall, the proposed model provides a more accurate representation of the MFCE than Models 1 and 2. Although its capability in capturing MFCE does not surpass that of Model 3 [23], the proposed model achieves competitive performance with a lower model order and thus reduced computational complexity. In addition, our model incorporates the grid side's dynamic characteristics, which are not considered in the original modeling framework presented in [23]. With these merits, our model is expected to be more applicable in practical grids with complex dynamic behaviors.

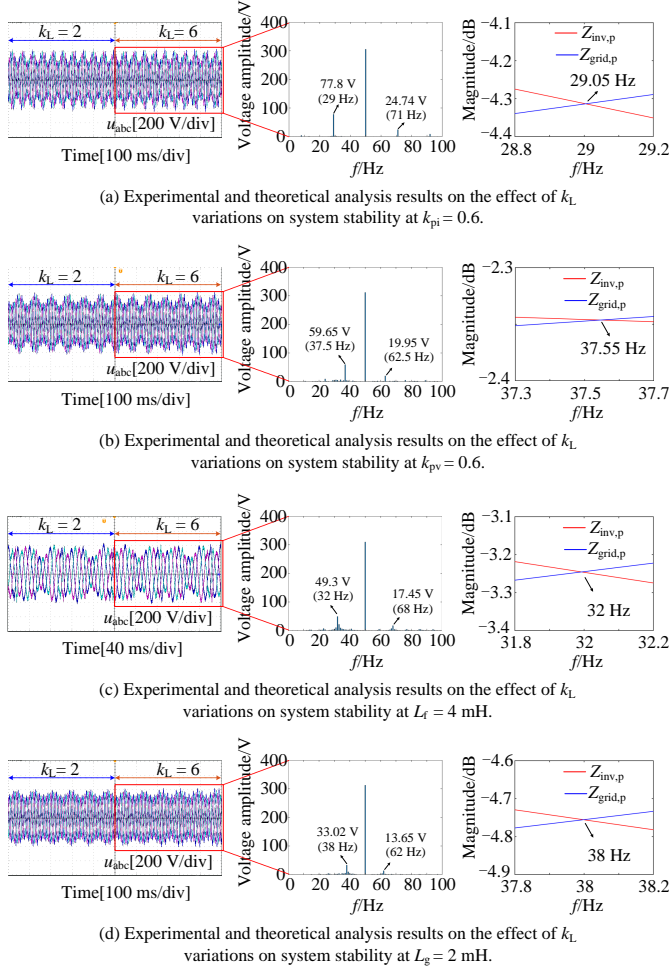


Fig. A5. Experimental and theoretical analysis result of the effect of  $k_L$  variations on system stability.

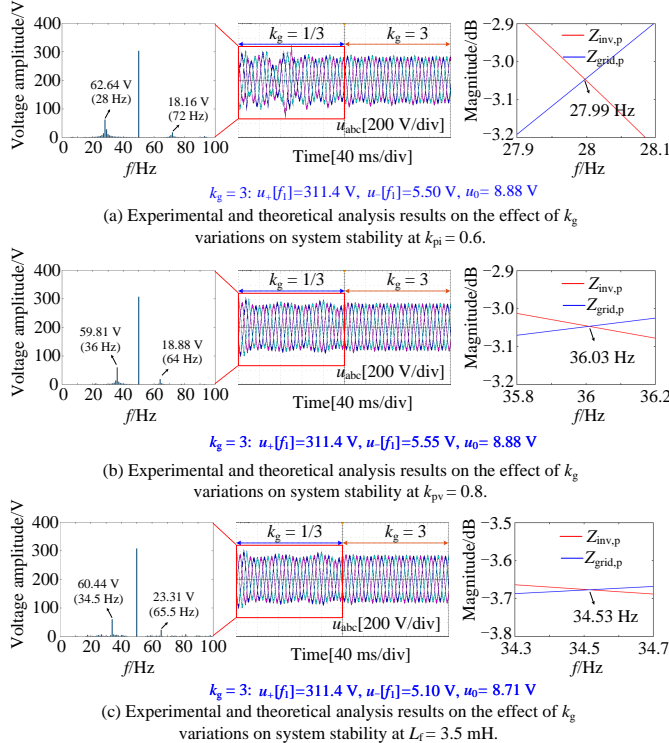


Fig. A6. Experimental and theoretical analysis result of the effect of  $k_g$  variations on system stability.